

Trapping of low-index microparticles in an optical vortex

K. T. Gahagan and G. A. Swartzlander, Jr.

Department of Physics, Worcester Polytechnic Institute, Worcester, Massachusetts 01609-2280

Received May 6, 1997; revised manuscript received October 6, 1997

The equilibrium position of a low-index particle in an optical-vortex trap was experimentally measured for two different systems: a buoyant hollow glass sphere in water and a density-matched water droplet in acetophenone. Vortex traps are the only known static, single-beam configurations allowing three-dimensional trapping of such particles in the size range of 2–50 μm . The trap consists of a strongly focused Gaussian laser beam containing a holographically produced optical vortex. Using experimental and theoretical techniques, we also explored changes in the trapping efficiency owing to the vortex core size, the relative refractive index, and the numerical aperture of the focusing objective. © 1998 Optical Society of America
[S0740-3224(98)03802-8]

OCIS codes: 350.3950, 080.0080.

1. INTRODUCTION

Gradient force optical traps,¹ also known as optical tweezers, have become a valuable tool for researchers in diverse fields, e.g., acoustics,² interface science,^{3–5} biology,^{6–9} and biophysics.^{10–13} Early three-dimensional trapping of a transparent, dielectric sphere was accomplished with a strongly focused TEM₀₀-mode Gaussian laser beam for a sphere having a relative refractive index greater than unity¹ (i.e., the refractive index of the trapped particle was greater than that of the surrounding medium). With increased interest in optical tweezers, certain limitations of this conventional gradient force trap have arisen. For instance, particles are trapped near the high-intensity focal region of the beam and thus are susceptible to optical damage through absorptive heating.^{14–16} Furthermore, multiple particles may be attracted into the same trap; hence isolating a single particle requires dilute samples. Absorbing particles larger than ~40 nm are knocked out of the trap owing to the impact of photons.¹⁷ What is more, the conventional stationary Gaussian-beam trap has thus far not succeeded in trapping spherical low-index particles such as bubbles and droplets.

An alternative trap design, which may overcome some of these limitations, was explored by Ashkin and others and involves replacing the TEM₀₀-mode beam with a beam containing an optical vortex. The optical-vortex beam is characterized by a dark spot within the intensity profile of the beam, owing to interference in the vicinity of the vortex-phase singularity^{18,19} (see Subsection 2.B). Efficient high-index particle traps with higher-order Laguerre–Gaussian-mode beams were achieved with an intracavity aperture^{20,21} within a laser, with external mode-converting optics,²² and with a computer-generated hologram (CGH).²³ Optical damage was reportedly minimized with such a beam.²¹ In addition, the special phase structure of the optical vortex has been shown to induce rotation in absorbing particles through angular-

momentum transfer from the vortex beam.^{23–26} The angular momentum of a vortex may also be used to control the motion of other vortices.^{27,28} We recently reported experiments showing that a stationary vortex beam could also be used to three-dimensionally trap low-index particles such as hollow glass spheres in water,²⁹ presenting an alternative to other more complicated techniques for trapping low-index particles with a rotating beam³⁰ or specially shaped micromachined particles.^{31,32}

In this paper, we describe theoretical and experimental investigations of the optical-vortex trap (OVT) for low-index particles. Section 2 provides a theoretical framework to discuss the OVT based on a ray-optics (RO) model. The trapping efficiency is described analytically and numerically for various parameters, such as the relative refractive index of the trapped particle, the numerical aperture of the focusing objective, and the relative size of the vortex core to the beam waist. Our experimental findings and procedures are reported in Section 3. Two low-index particle systems are analyzed: hollow glass spheres in water (12–36- μm diameter) and water droplets in acetophenone (4–20 μm diameter). Comparisons of our experimental findings with predictions based on a RO model are reported in Section 4 along with a discussion of some practical considerations, followed by conclusions in Section 5.

2. THEORY

Optical traps have been modeled by electromagnetic wave^{33–35} and RO^{20,36} representations, as well as hybrid models with elements from both approaches.³⁷ The success of these respective models is largely dependent on the size of the particles under consideration and the cone angle of the focused beam. If both the wavelength λ and focal-spot radius w_f of the trapping beam are much smaller than the particle radius R_p , the stationary-phase approximation may be used to justify a simple model

based on geometrical optics to calculate the trapping efficiency (see, for example, van de Hulst³⁸). These conditions ($R_p \gg \lambda$, w_f) are satisfied for the systems studied here.

A. Ray-Optics Model

An ideal infinite conjugate-ratio microscope objective may be used to focus a planar monochromatic beam incident at the input aperture of the objective to a diffraction-limited spot in the object plane. We consider a beam propagating downward in the $+z$ direction and, for convenience, define the plane $z = 0$ to coincide with the focal plane of the beam in the object space. Hence the axial position of a particle will be negative if it is located above the focus. For example, a low-index particle may be stably trapped within the dark core of the optical vortex at a point $z_{\text{trap}} < 0$ [see Fig. 2(b)]. Ignoring diffraction effects, the focused beam may be treated as a bundle of rays that intersect at a point in the front focal plane. The trajectory of the m^{th} ray in an initially collimated bundle, shown in Fig. 1(a), is characterized by the coordinates (ρ_m, ϕ_m) at the objective input aperture and (γ_m, ϕ_m) in the focal region. The angle γ_m is given by $\gamma_m = \tan^{-1}[\tan \gamma_{\text{max}} \times (\rho_m/\rho_a)]$, where $\gamma_{\text{max}} = \sin^{-1}(\text{NA}/n_0)$ is the cone angle, NA is the numerical aperture of the objective, n_0 is the index of refraction of the medium in the focal region, and ρ_a is the radius of the input aperture of the objective. We use a Zeiss Neofluar oil-immersion objective (NA = 1.3) to trap particles immersed in either water ($n_0 = 1.33$) or acetophenone ($n_0 = 1.53$). The corresponding cone angles for beams focused in these media are 78° and 58° , respectively.

To determine the power associated with each ray, the input aperture is divided into discrete regions of area A_m , and one ray is assigned to each region. The power P_m associated with the ray is given by $P_m(\rho_m, \phi_m) = \langle I_m(\rho_m, \phi_m) \rangle A_m$, where $\langle I_m \rangle$ is the average intensity of the input beam in the m^{th} region. By scaling the ray power to the localized intensity, we ignore the phase profile of the beam and hence also the electromagnetic angular momentum of the vortex. The momentum of each photon in the ray is given by $\hbar \mathbf{k}^{(m)}(\phi, \gamma)$, with magnitude $\hbar k$, where $k = 2\pi n_0/\lambda$ is the wave number of the beam

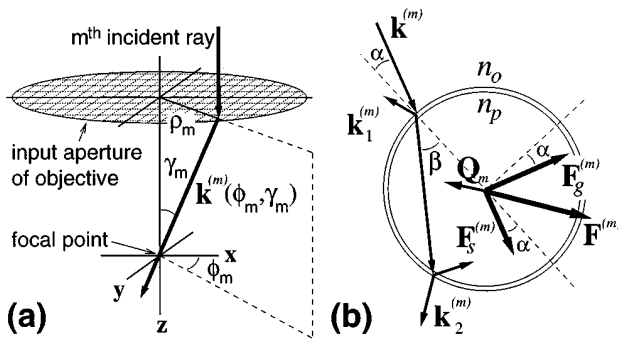


Fig. 1. (a) Trajectory for an arbitrary ray normally incident at the input aperture of the focusing objective. (b) View of the plane of incidence for a single ray with incident wave vector $\mathbf{k}^{(m)}$ striking a low-index particle ($n_p/n_0 \leq 1$). The change in momentum resulting from reflection and refraction gives rise to a radiation pressure force $\mathbf{F}^{(m)} = \mathbf{F}_s^{(m)} + \mathbf{F}_g^{(m)}$.

in the continuous medium. A ray incident on a dielectric particle will be multiply reflected and refracted at the particle surface, thereby transferring momentum between the electromagnetic field and the particle. The resulting radiation pressure force on the particle may be written as

$$\begin{aligned} \mathbf{F}^{(m)} &= \frac{n_0 P_m}{c} \left[\hat{\mathbf{k}}^{(m)} - \mathcal{R}_m \hat{\mathbf{k}}_1^{(m)} - \mathcal{T}_m^2 \sum_{i=2}^{\infty} \mathcal{R}_m^{(i-2)} \hat{\mathbf{k}}_i^{(m)} \right] \\ &= \frac{n_0 P_m}{c} \mathbf{Q}_m, \end{aligned} \quad (1)$$

where the terms $\hat{\mathbf{k}}_i^{(m)}$ are unit vectors in the directions of the reflected and refracted rays, \mathcal{R}_m and \mathcal{T}_m are the power reflectance and transmittance of the ray at the particle surface and c is the speed of light in vacuum. \mathbf{Q}_m , representing the sum of terms in brackets, may be identified as the radiation pressure efficiency of the m^{th} ray. Figure 1(b) depicts the plane of incidence for a ray striking a low-index ($n_p < n_0$) spherical dielectric particle, showing the first reflected ray, $\mathbf{k}_1^{(m)}$, and the first refracted ray, $\mathbf{k}_2^{(m)}$. The angles α and β are the incident and refracted angles of the ray with respect to the normal to the surface (dashed line). Following Ashkin's formalism,²⁰ it is convenient to decompose the force into the two components depicted in Fig. 1(b): the scattering force $\mathbf{F}_s^{(m)}$, which is directed parallel to the incident ray, and the gradient force $\mathbf{F}_g^{(m)}$, which is directed perpendicular to the incident ray. Roosen³⁶ has derived closed-form expressions for the magnitude of these components, given by

$$\mathbf{F}_s^{(m)} = [\mathbf{F}^{(m)} \cdot \hat{\mathbf{k}}^{(m)}] \hat{\mathbf{k}}^{(m)}, \quad (2)$$

$$\begin{aligned} F_s^{(m)} &= \frac{n_0 P_m}{c} \left\{ 1 + \mathcal{R}_m \cos(2\alpha) \right. \\ &\quad \left. - \frac{\mathcal{T}_m^2 [\cos(2\alpha - 2\beta) + \mathcal{R}_m \cos(2\alpha)]}{1 + \mathcal{R}_m^2 + 2\mathcal{R}_m \cos(2\beta)} \right\}, \end{aligned} \quad (3)$$

$$\mathbf{F}_g^{(m)} = \hat{\mathbf{k}}^{(m)} \times [\mathbf{F}^{(m)} \times \hat{\mathbf{k}}^{(m)}], \quad (4)$$

$$\begin{aligned} F_g^{(m)} &= \frac{n_0 P_m}{c} \left\{ \mathcal{R}_m \sin(2\alpha) \right. \\ &\quad \left. - \frac{\mathcal{T}_m^2 [\sin(2\alpha - 2\beta) + \mathcal{R}_m \sin(2\alpha)]}{1 + \mathcal{R}_m^2 + 2\mathcal{R}_m \cos(2\beta)} \right\}. \end{aligned} \quad (5)$$

We note that the parameters \mathcal{T}_m , \mathcal{R}_m , α , and β depend on the relative refractive indices of the particle and host, as well as the polarization of the beam. For simplicity, we assume an axially symmetric, circularly polarized beam for which the trapping force is likewise axially symmetric and may be characterized by a single transverse component. If the refractive index of the medium in the focal region differs from that of the immersion medium and microscope coverslip ($n \approx 1.52$), rays incident at different angles γ_m will not intersect in the same plane, thereby forming a caustic. Furthermore, the optical power reflected at the interface between the coverslip and the medium increases as γ_m increases, causing apodization of the beam. Such effects are exaggerated when the

focus is far below the coverslip and for high numerical apertures and may be included as refinements to the RO model.

The net force on a particle, \mathbf{F}_{net} , is calculated by summing the contributions of the individual rays. To carry out this summation, it is convenient to transform Eqs. (3) and (5) to the laboratory coordinate system (γ_m, ϕ_m) defined in Fig. 1(a). The longitudinal and transverse components of the force for the m^{th} ray are

$$\begin{aligned} F_z^{(m)} &= \pm F_g^{(m)} \sin \gamma_m + F_s^{(m)} \cos \gamma_m \\ &= F_{gz}^{(m)} + F_{sz}^{(m)}, \end{aligned} \quad (6)$$

$$\begin{aligned} F_\rho^{(m)} &= [\pm F_g^{(m)} \cos \gamma_m + F_s^{(m)} \sin \gamma_m] \cos \phi_m \\ &= F_{g\rho}^{(m)} + F_{s\rho}^{(m)}, \end{aligned} \quad (7)$$

where the subscripts g and s refer to the gradient and scattering force contributions, respectively. The \pm sign of the gradient force terms, which depends on the position of the particle center relative to the beam focus and the incident-ray trajectory, may be determined unambiguously from Eq. (4). Suppose, for instance, that the particle pictured in Fig. 1(b) is centered on the optical axis above the focal plane. In this case, the sign of the transverse component of the gradient force $\mathbf{F}_{g\rho}^{(m)}$ is positive (away from the optical axis). On the other hand, the longitudinal component $\mathbf{F}_{gz}^{(m)}$ is negative (opposite the direction of propagation).

Finally, the net force may be written $\mathbf{F}_{\text{net}} = \sum_{(m)} \times [F_\rho^{(m)} \hat{\rho} + F_z^{(m)} \hat{z}]$. Later we will compare the trapping efficiency of different configurations, and thus we normalize the forces with respect to the total beam power, $P = \sum_m P_m$. The trapping efficiency is defined as the dimensionless quantity $\mathbf{Q} = (c/n_0 P) \mathbf{F}_{\text{net}} = Q_\rho \hat{\rho} + Q_z \hat{z}$, where the transverse and longitudinal components of the efficiency are Q_ρ and Q_z , respectively. Note that except in the case of a uniform beam intensity, such that all P_m are equal, that $\mathbf{Q} \neq \sum_m \mathbf{Q}_m$. To facilitate an understanding of the separate gradient (g) and scattering (s) effects, one may decompose \mathbf{Q} :

$$Q_{s\rho} = (c/n_0 P) \sum_{(m)} F_{s\rho}^{(m)}, \quad (8)$$

$$Q_{sz} = (c/n_0 P) \sum_{(m)} F_{sz}^{(m)}, \quad (9)$$

$$Q_{g\rho} = (c/n_0 P) \sum_{(m)} F_{g\rho}^{(m)}, \quad (10)$$

$$Q_{gz} = (c/n_0 P) \sum_{(m)} F_{gz}^{(m)}. \quad (11)$$

B. Optical Vortex Trap

Stable three-dimensional trapping requires a balance between the optical gradient and scattering forces to form a potential well sufficiently deep to overcome mechanical forces owing to buoyancy, viscous drag, or Brownian motion. Optical trapping of high-index dielectric particles in liquid ranging in size from several nanometers to tens of microns in diameter has been demonstrated with a single beam focused with a high NA microscope

objective.¹ Trapping of gaseous clouds of cold atoms has also been demonstrated with a single focused beam.¹ Near the upper size limit, gravitational or buoyant forces and viscous drag are primarily responsible for trap destabilization. In principle, these forces may be overcome by delivering more optical power to the focal region, although this is not always feasible if optical damage is a concern. The use of a hollow beam such as an optical vortex allows more efficient trapping,^{20,21} thus reducing the risk of optical damage. Trapping of both high²⁰ and low²⁹ refractive-index particles with an optical vortex has been demonstrated.

A monochromatic optical-vortex beam with frequency $\omega = kc/n_0$ propagating in the $+z$ direction may be characterized by a scalar electric field, $E = A \exp(i\omega t - ikn_0 z)$, where the envelope is $A = A_0(\rho, \phi, z) \times \exp(iM\phi)$, where M is an integer called the topological charge, which is unity in this paper. If the amplitude is cylindrically symmetric, then, because of destructive interference, the beam is characterized by a dark central core in both the near- and far-field regions with $A(\rho = 0) = 0$. The calculated intensity profile of a vortex beam is depicted in Fig. 2(a), where we have assumed an amplitude

$$A_0 \approx E_0 \exp(-\rho^2/w_0^2) \tanh(\rho/w_v), \quad (12)$$

where w_0 corresponds to the size of a Gaussian beam at the input face of the objective and w_v is the characteristic core size.

The longitudinal and transverse trapping efficiencies may be numerically determined from Eqs. (8)–(11). As one example, consider a low-index water droplet in acetophenone ($n_p/n_0 = 1.33/1.53 = 0.87$) and a beam with vortex core size $w_v = 0.1w_0$. Refractive-index matching between the coverslip and acetophenone permits us to ignore defocusing and apodization effects at the interface. The vortex beam is assumed to fill the input aperture such that $w_0 = \rho_a$. Figure 2(b) depicts the water droplet trapped at the point z_{trap} in the core of the vortex.

A vector plot of the efficiency \mathbf{Q} in a vertical plane containing the optical axis (see Fig. 3) clearly shows a stable equilibrium position at a point $z_{\text{trap}} \approx -2.54R_p$. The arrows in Fig. 3 represent the trapping efficiency for a spherical droplet centered at the position of the tail of the arrow and are logarithmically scaled according to the scale located in the upper-right corner of the figure. The shaded hemisphere represents a trapped droplet of radius R_p drawn to scale. The dashed line represents the edge of the vortex core, w_v , while the solid line denotes the

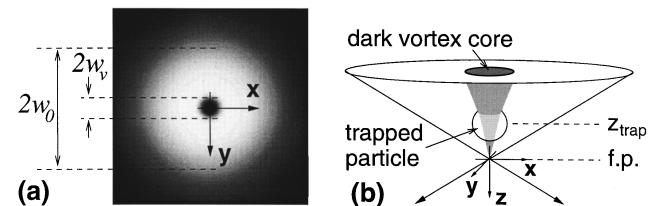


Fig. 2. (a) Intensity profile of a vortex beam with beam waist w_0 and vortex waist w_v at input aperture of focusing objective. (b) Diagram of stable trapping configuration for a low-index particle in an OVT. Diagram is drawn to scale for a water droplet in acetophenone trapped with $\text{NA} = 1.3$ and $\eta = 0.1$.

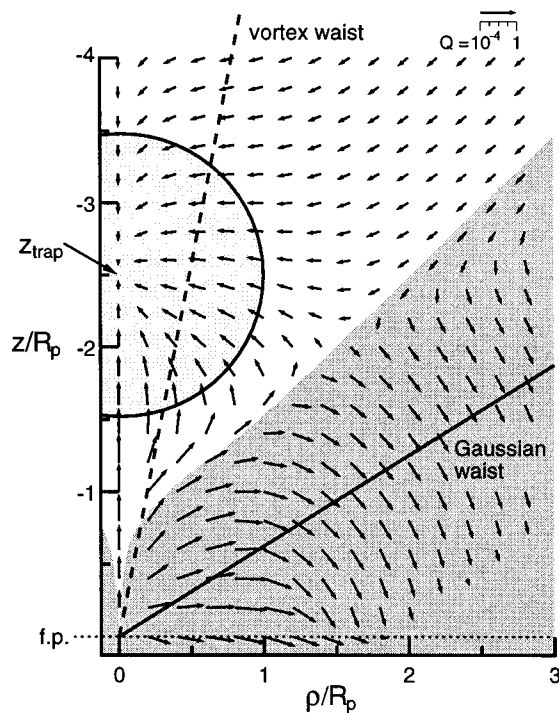


Fig. 3. Vector representation of the trapping efficiency for an OVT with $n = 0.9$, $\eta = 0.1$, and $\text{NA} = 1.3$ in a vertical plane containing the optical axis. Coordinates are scaled in units of the particle radius R_p . The length of the arrows scales logarithmically with the efficiency according to the scale depicted in the upper-right corner of the figure. The tail of the arrows marks the position of the particle center.

edge of the Gaussian envelope, w_0 . The large shaded region denotes the area in which particles will be repelled by the beam rather than attracted into the trap. It is clear from Fig. 3 that no part of the particle intersects the focal plane, however, the particle is exposed to some radiation. Furthermore, the trapping force is weakest at points on the optical axis above z_{trap} as may be expected, owing to the low intensity in the vicinity of the vortex core as well as lower intensities in the broadened beam. This weak region represents a possible capture or escape route for trapped particles and thus merits a more detailed investigation.

Figure 4(a) plots the calculated scattering and gradient efficiencies Q_{sz} and Q_{gz} , as well as the net longitudinal efficiency $Q_z = Q_{sz} + Q_{gz}$ for a droplet centered on the optical axis ($\rho = 0$). At $z = z_{\text{trap}}$, the scattering and gradient forces are in equilibrium. Above the equilibrium position ($z < z_{\text{trap}}$), the scattering term Q_{sz} dominates, and the droplet is subjected to a restoring force pushing it down toward z_{trap} . For $z > z_{\text{trap}}$, the gradient term Q_{gz} dominates, and the restoring force is upward. This trapping scheme differs from that of a conventional gradient-force trap for high-index particles, in which the intensity gradient provides a restoring force both above and below the stable point. In contrast to the detrimental effect of scattering in a conventional high-index trap, low-index vortex trapping is improved by, and in fact requires, a strong longitudinal scattering force.

The relative increase in the gradient force below z_{trap} may be understood by considering the solid angle of rays

striking the particle. From Eqs. (6) and (7), the ratio of longitudinal forces exerted by a ray incident at an angle γ_m is $|F_{gz}^{(m)}|/|F_{sz}^{(m)}| = (F_g^{(m)}/F_s^{(m)})\tan \gamma_m$. Accordingly, large angle rays will tend to contribute more strongly to the longitudinal gradient force than to the longitudinal scattering force. As the particle is translated downward along the optical axis, the solid angle of rays intersecting the particle increases, favoring the gradient force.

The calculated transverse efficiency in the trapping plane $Q_\rho(z_{\text{trap}})$ is plotted in Fig. 4(b). The individual contributions from the scattering and gradient forces, $Q_{s\rho}$ and $Q_{g\rho}$, show that both terms contribute to a restoring force. The droplet experiences the maximum transverse restoring force at $\rho = 0.8R_p$. Further from the optical axis (beyond $\rho = 2.5R_p$) the efficiency becomes positive, and the droplet is pushed out of the beam. Actually, repulsion of the droplet occurs somewhat closer to the axis at $\rho = 2.0R_p$ (see Fig. 3) owing to longitudinal force components not accounted for in Fig. 4(b). This reversal results from a change in the intensity gradient incident on the droplet as it moves away from the optical axis. Near the axis, the gradient pushes the droplet toward the low-intensity vortex core. For larger transverse displacements, the gradient of the Gaussian envelope pushes the droplet out of the beam. This phenomenon may be advantageously used to isolate a single trapped particle from other particles in the system. Rather than surmounting the potential barrier in the transverse direction, a particle may most easily enter the trap if it lies along the optical axis at points $z < z_{\text{trap}}$.

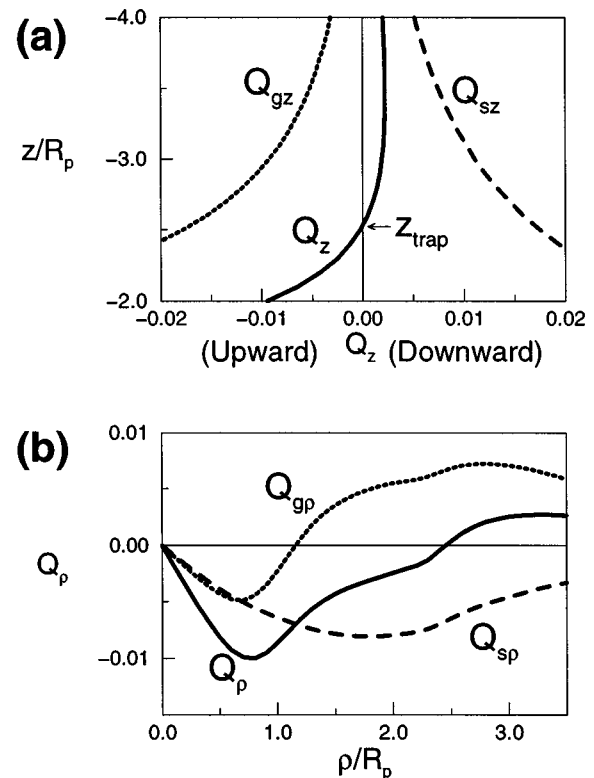


Fig. 4. (a) Longitudinal and (b) transverse components of the trapping efficiency along the axis ($\rho = 0$) and in the plane $z = z_{\text{trap}}$, respectively ($n = 0.9$, $\eta = 0.1$, and $\text{NA} = 1.3$).

Readers familiar with the conventional gradient-force trap will undoubtedly notice that the efficiency for trapping low-index particles in the OVT is about an order of magnitude smaller than typical values for trapping of high-index particles. This fact should not be interpreted to mean that optical damage is more likely in the OVT. In fact, for the trapped droplet pictured in Fig. 3, only 12% of the total beam power strikes the particle, hence the effective efficiency is 1/0.12 times larger than that calculated with the power of the entire beam.

C. Parametric Considerations

We now consider the effect of varying individual parameters such as the ratio of vortex to beam size, $\eta = w_v/w_0$, the NA of the focusing objective, and the relative refractive index, $m = n_p/n_0$. Initially, we assume $w_0 = \rho_a$ is a fixed value (i.e., NA is constant) and that the vortex size may be varied (for example, by designing different CGH's). From the discussion of Fig. 4(a), one may expect the core size to affect the stability and efficiency of the vortex trap. Normalized beam profiles with η equal to 0.3, 0.2, 0.1, and 0.0 (Gaussian) are depicted in Fig. 5. In principle, the vortex cores will diffract. However, with CGH's it is possible to achieve a profile characterized by Eq. (12) in the vicinity of the trapped particle. The on-axis longitudinal efficiency $Q_z(\rho = 0)$ is plotted in Fig. 6(a) for each of these profiles, with $m = 0.87$. Surprisingly, the equilibrium position remains nearly constant for these cases at $z_{\text{trap}} = (-2.54 \pm 0.02)R_p$. This invariance results from a complicated angular dependence of the longitudinal force exerted by individual rays and is explained in more detail at the end of this section. We also see that the efficiency $Q_{z,\text{max}}$ along the escape corridor increases as η decreases, as expected from the greater portion of the beam power striking the particle. The desired value of $Q_{z,\text{max}}$ for a particular trapped particle depends on the escape mechanism.

While a larger vortex core weakens the trap in the longitudinal direction, we find that it strengthens the trap in the transverse direction. This effect is shown in Fig. 6(b), which depicts the efficiency $Q_\rho(\rho, z_{\text{trap}})$ in the trap-

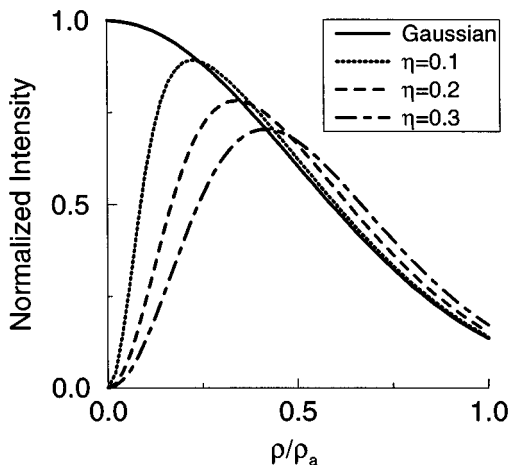


Fig. 5. Intensity profiles for η equal to 0.0 (Gaussian), 0.1, 0.2, and 0.3 are normalized with respect to the total beam power and scaled to the input aperture radius ρ_a .

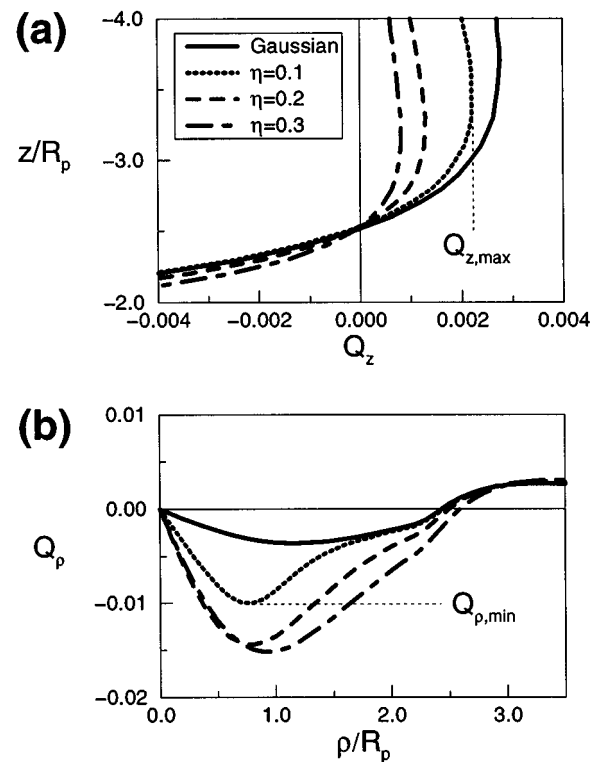


Fig. 6. (a) $Q_z(\rho = 0)$ and (b) $Q_\rho(z = z_{\text{trap}})$ for relative vortex core sizes, η equal to 0.0, 0.1, 0.2, and 0.3. Legend applies to both graphs.

ping plane. As η increases from zero to 0.2, the minimum efficiency $Q_{\rho,\text{min}}$ (corresponding to the maximum restoring force) decreases from -0.005 to -0.015 and then appears to saturate. The outward radial shift of $Q_{\rho,\text{min}}$ for $\eta = 0.3$ is attributed to the increased width of the vortex core. Comparing Figs. 6(a) and 6(b), we see that transverse trapping is roughly an order of magnitude stronger than longitudinal trapping.

Variation of NA also affects the OVT. The longitudinal and transverse efficiencies as a function of NA are shown in Figs. 7(a) and 7(b), respectively. As before, we plot $Q_z(\rho = 0)$ and $Q_\rho(z_{\text{trap}})$ with $\eta = 0.1$ and $m = 0.87$. From Fig. 7(a), we see that NA does not significantly affect the location of z_{trap} , yet it has a pronounced effect on the magnitude of Q_z , particularly along the escape corridor, which is strengthened for smaller values of NA. The strengthening effect is attributed to the redistribution of beam power to the paraxial region as NA decreases. The invariance of z_{trap} with NA suggests that, as with η , the redistribution of beam power affects only the magnitudes and not the balance between the gradient and scattering forces near z_{trap} .

From Fig. 7(b), we observe that for NA = 1.0, the trap is unstable with no restoring force in the transverse plane. In contrast, for a conventional trap for high-index particles the onset of trap instability with decreasing NA occurs in the longitudinal direction. As NA increases to 1.3, the minimum efficiency $Q_{\rho,\text{min}}$ decreases to 0.01. The increased transverse restoring force results from the shift of beam energy to rays incident at larger values of γ_m . The saturation results from the beam energy shifting to rays that do not strike the particle. The increased

cone angle is also responsible for the increase in the radial position of $Q_{\rho, \min}$ at $NA = 1.3$, effectively widening the trap.

According to the calculations depicted in Fig. 6, both the vortex and Gaussian beams are predicted to stably trap low-index particles. In practice, however, we have not been able to trap low-index particles with a Gaussian trap; rather, the particle escapes in the transverse plane. Numerical calculations for a Gaussian trap, with conditions otherwise identical to those used to obtain Fig. 7, support this experimental finding. Indeed, the Gaussian trap is unstable unless $NA > 1.23$. In comparison, the threshold for a vortex trap is $NA = 1.08$ (for $\eta = 0.1$). Although we use an objective with a nominal value of $NA = 1.30$, diffraction at the pupil edges and apodization by the coverslip may decrease the effective cone angle of the beam. Thus, for a Gaussian trap, the stable trapping region, if formed, will be weak. Although higher NA objectives ($NA = 1.4$, for example) are commercially available, the small working distance makes trapping more difficult for some applications.

The final parameter we consider is the effective refractive index, $m = n_p/n_0$. Figure 8(a) plots Q_z along the optical axis for several values of m with $\eta = 0.1$ and $NA = 1.3$ held fixed. In contrast to our previous analyses, in which the trapping position was relatively stationary as we varied η and NA , here we see in Fig. 8(a) that the equilibrium position shifts further away from the beam focus

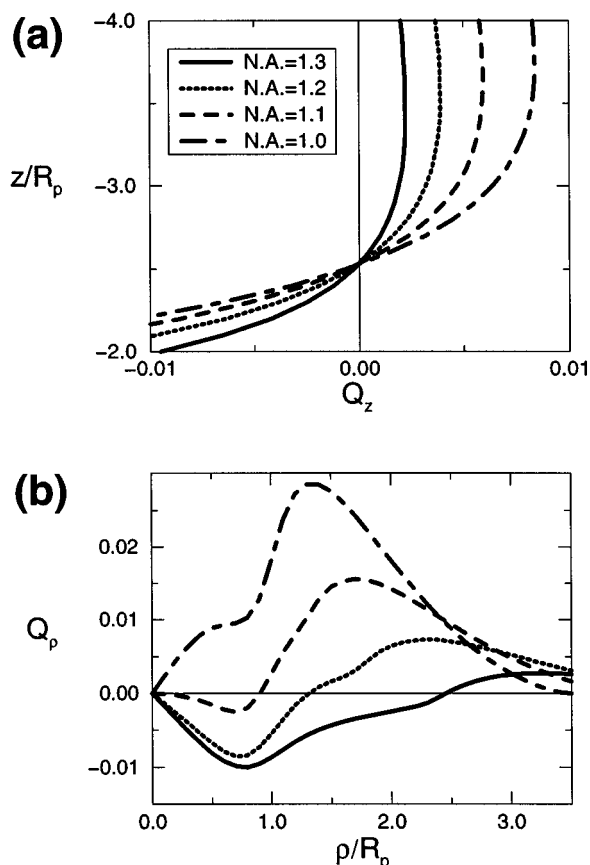


Fig. 7. (a) $Q_z(\rho = 0)$ and (b) $Q_\rho(z = z_{\text{trap}})$ for numerical apertures of 1.0, 1.1, 1.2, and 1.3. Legend applies to both graphs.

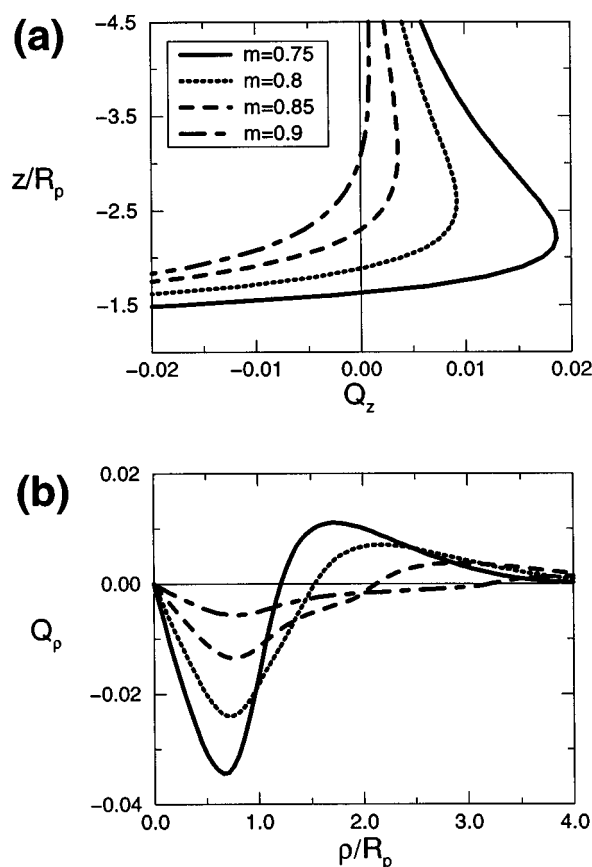


Fig. 8. (a) $Q_z(\rho = 0)$ and (b) $Q_\rho(z = z_{\text{trap}})$ for relative refractive-index values m equal to 0.75, 0.8, 0.85 and 0.9. Note the strong dependence of the stable trapping position on m . Legend applies to both graphs.

as m decreases. This effect was easily observed experimentally. The strengthening of the trap in the escape region with increasing m , also shown in Fig. 8, results from an increase in the exposure of the particle to light as it shifts closer to the beam focus and from an increase in the power reflectance.

In the transverse trapping plane $z = z_{\text{trap}}$, an increase in m strengthens the OVT, while simultaneously decreasing its width, as shown in Fig. 8(b). Both effects result from the shift of z_{trap} toward the beam focus where the beam is both narrower and more intense. These effects suggest a trade-off between trapping efficiency and stability. For larger m , the trapping efficiency increases, but the particle is also trapped closer to the beam focus where the transverse dimensions of the trapping region are smaller. A small transverse displacement of the particle that is due to Brownian motion or an applied transverse force can more easily move the particle beyond the boundary of the trap.

Before describing our experimental characterization of the OVT, let us examine in more detail the dependence of z_{trap} on the various parameters η , NA , and m . A deeper understanding of these trends may be reached by examining the dependence of the longitudinal forces exerted by each incident ray on the angle γ_m between the ray and the axis. Figure 9 depicts the longitudinal components of the ray efficiency, $Q_m(\gamma_m)$, for a water droplet in ac-

etophenone at the stable point $z_{\text{trap}} = -2.54R_p$. As expected, the ray-gradient efficiency $Q_{gz}^{(m)}$ is negative, while the ray-scattering efficiency $Q_{sz}^{(m)}$ is positive for all γ_m , and each efficiency reaches a peak magnitude near $\gamma_m \approx 21^\circ$. This peak corresponds closely to the critical angle, $\gamma_c = 20^\circ$ ($\alpha_c = 60^\circ$), for total reflection of the incident beam. The truncation of the efficiency for $\gamma_m > 23.8^\circ$ corresponds to the limit of the cone of rays striking the particle. The longitudinal efficiency for the ray, $Q_z^{(m)} = Q_{gz}^{(m)} + Q_{sz}^{(m)}$, is more interesting and is characterized by alternating regions of positive and negative efficiency as γ_m increases.

The net longitudinal efficiency for all rays may be determined by computing the weighted sum $Q_z = (1/P)\sum_m P_m Q_z^{(m)}$ and will become zero at the stable point. Thus any beam with a set of weighting factors (i.e., power distribution) for which the sum is zero may have a stable point at $z_{\text{trap}} = -2.54R_p$. Indeed, this is approximately the case for the beam profiles we have considered. For instance, as the core size increases, beam power shifts to rays with larger values of γ_m . A loss of downward force contributed by rays near the axis ($\gamma_m < 10^\circ$), is compensated by a gain in downward force from rays in the positive region $19^\circ < \gamma_m < 22^\circ$. Similar compensation occurs in regions of upward force. In addition, a fraction of the incident power is shifted to the region above the cutoff at $\gamma_m = 23.8^\circ$, reducing the magnitude of the efficiency. Thus variations in η or NA, which change the angular distribution of the incident beam, do not strongly alter z_{trap} , but may influence the trapping efficiency.

Variation of the refractive index m , on the other hand, requires a shift in z_{trap} to restore a balance between the gradient and scattering forces. The ray efficiency for the case $m = 0.75$ in the plane $z = -2.54R_p$ is depicted in

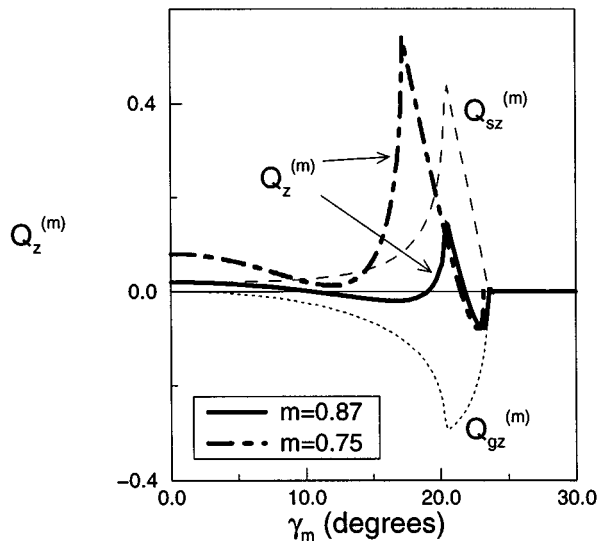


Fig. 9. Ray efficiency $Q_z^{(m)}$ for an individual ray incident at an angle γ_m on a particle located at $z_{\text{trap}} = -2.54R_p$ ($m = 0.87$, $\eta = 0.1$, and $\text{NA} = 1.3$). The dotted and dashed curves refer to $Q_{gz}^{(m)}$ and $Q_{sz}^{(m)}$, respectively. The solid and dotted-dashed curves correspond to the total longitudinal ray efficiency for two different values of m , as indicated in the legend.

Fig. 9 for comparison. The increased reflectivity of the particle surface is seen to favor the scattering force at small angles γ_m . To compensate, the particle may shift downward to increase the solid angle of rays striking the particle, thereby increasing the upward gradient force. As we will demonstrate, this trend is consistent with our experimental observations.

3. EXPERIMENT

We now present experiments conducted in our laboratory to characterize the OVT. With the experimental apparatus described below, we have studied two different low-index particles systems. Our results confirm many of the parametric trends predicted by the RO model.

A. Setup

The experimental apparatus used to create the OVT is shown in Fig. 10. A Gaussian beam from an argon-ion laser (Ar^+) at wavelength $\lambda = 514 \text{ nm}$ is directed first through a beam expander (BX1) and then through a computer generated hologram (CGH), which places an optical vortex of charge $M = 1$ onto the first-order diffracted beam. The collimated first-order diffracted beam passes through a second beam expander (BX2) before entering a $100\times$, $\text{NA} = 1.30$, Zeiss Neofluar oil-immersion microscope objective (Obj) with an input aperture of diameter $\sim 2w_0$. A sample chamber containing the particle system is placed at the focus of the objective and backlit by a white-light source. The particles are viewed through the same $100\times$ objective by means of a beam splitter (BS), an imaging lens (L), a video camera (CCD), and a television monitor (TV). Video sequences were recorded with a Macintosh computer and a video-cassette recorder. The beam expanders (BX1 and BX2) permit adjustment of the relative core size η while maintaining a fixed beam waist at the input aperture. The imaging lens (L) was arranged to collimate the light from the objective to allow scanning of the z position of the image plane relative to the beam focus while maintaining constant image scaling. This permitted easy measurement of the trap position relative to the beam focus, z_{trap} , as a function of particle size. A second CCD camera (CCD2), placed at the same distance from the beam splitter as the input face of the objective, was used to record the intensity profile at the input aperture of microscope objective. A power meter placed in front of CCD2 and calibrated to the power transmitted by the objective was used to estimate the power of the trapping beam.

B. Preparation of Low-Index Particle Systems

Two low-index particle systems were studied with this setup. The first system consists of an emulsion of water droplets ($n_p = 1.33$, $\rho = 1.00 \text{ g/mL}$) in acetophenone ($n_0 = 1.53$, $\rho = 1.02 \text{ g/mL}$). Sorbitan monooleate (Span 80, 5% wt.) was added to the acetophenone to help stabilize the emulsion and prevent adhesion of water droplets to the cover glass. Deionized water was then added to the acetophenone-Span mixture to give a 20% volume fraction for the dispersed water phase. The mixture was shaken vigorously to form an emulsion of spherical droplets ranging in diameter from $40 \mu\text{m}$ down to a few hun-

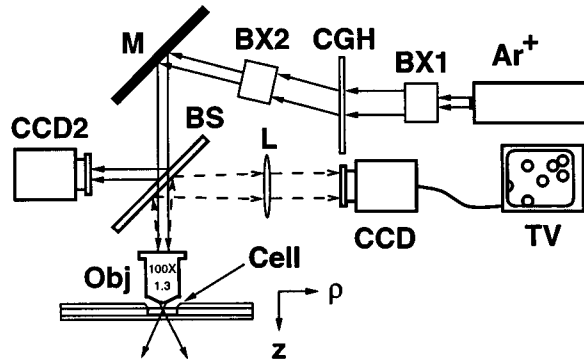


Fig. 10. Optical trap created by passing an Ar^+ laser beam through a computer-generated hologram (CGH) of an optical vortex. The beam is focused with a microscope objective (Obj) into a sample chamber (Cell) containing a low-index particle system. Beam expanders (BX1, BX2) permit variation of η , and the beam profile is monitored with a CCD camera (CCD2). The particle system is imaged through the same objective onto a second camera (CCD). A collimating lens (L) allows z scanning of the image plane. BS, beam splitter; M, mirror.

dred nanometers. To obtain a majority of particles with radii in the desired 2–10- μm range, the emulsion was poured into a graduated cylinder and allowed to settle for approximately 10 min. During this time, the larger water droplets floated to the top of the cylinder. Samples extracted from the region near the surface of the emulsion contained droplets of the desired size.

The second system of low-index particles consists of hollow glass spheres (HGS's) (R_p of 5–15 μm) in deionized water with a small amount of surfactant ($\leq 1\%$ wt. Tween 80) added to reduce electrostatic interaction between the spheres and the cover glass. If the glass shell of the sphere is thin compared with the radius, the refractive index may be approximated as that of an air bubble ($n_p \approx 1.0$). An estimate of the thickness is possible with knowledge of the average density of the hollow spheres. The manufacturer-specified average density $\rho_{\text{HGS}} = 0.2 \text{ g/cm}^3$ corresponds to a wall thickness of $t \approx 0.03R_p$, assuming t is a linear function of R_p , such that

$$t = R_p \left[1 - \left(\frac{\rho_{\text{HGS}} - \rho_{\text{glass}}}{\rho_{\text{air}} - \rho_{\text{glass}}} \right)^{1/3} \right], \quad (13)$$

where $\rho_{\text{glass}} = 2.45 \text{ g/cm}^3$ and $\rho_{\text{air}} = 1.2 \times 10^{-3} \text{ g/cm}^3$ are the densities of the glass wall and air, respectively. Using a microscope, we estimated a thickness of $t/R_p \approx 0.05 - 0.1$.

For both particle systems, a net buoyancy caused the particles to collect just below the glass cover slip placed on top of the liquid-filled chamber. Trapping was achieved by moving the beam focus up from below a particle until the particle was pushed down into the trap by the scattering force. Once in the trap, the particles could be translated horizontally or vertically, usually through the entire 120- μm height of the chamber. In some instances, attractive Van der Waals' forces between the particle and the cover slip were difficult to overcome. We found it beneficial in these cases to first inversely levitate the particle off the cover slip before trapping. This was accomplished by placing the beam focus above the par-

ticle, then moving the focus downward until the particle was freed from the upper surface. The particle was thus trapped on the lower side of the beam focus in a manner analogous to optical levitation.³⁹ Levitation is distinct from three-dimensional trapping in that the radiation pressure forces alone do not form a stable three-dimensional trap. Instead, a restoring force in the longitudinal direction is provided by buoyancy. Once levitated for a few seconds, the electrostatic attraction of the particle with the cover slip is usually reduced to a point where trapping above the beam focus is possible. This reduction may be attributed to layers of surfactant forming on the surface of the particle and cover slip.

C. Results

Figure 11 depicts a sequence of images recorded with the CCD camera (CCD) showing an example of three-dimensional trapping (of a water droplet in acetophenone, in this case). The imaging lens (L) was adjusted to focus the image of the trapped droplet, located in the plane $z = z_{\text{trap}}$, onto the CCD. By translating the sample cell with respect to the microscope objective, relative motion between the trapped droplet and the surrounding medium was achieved. The trapped droplet, marked with an arrow in the first frame, remains in focus and at the

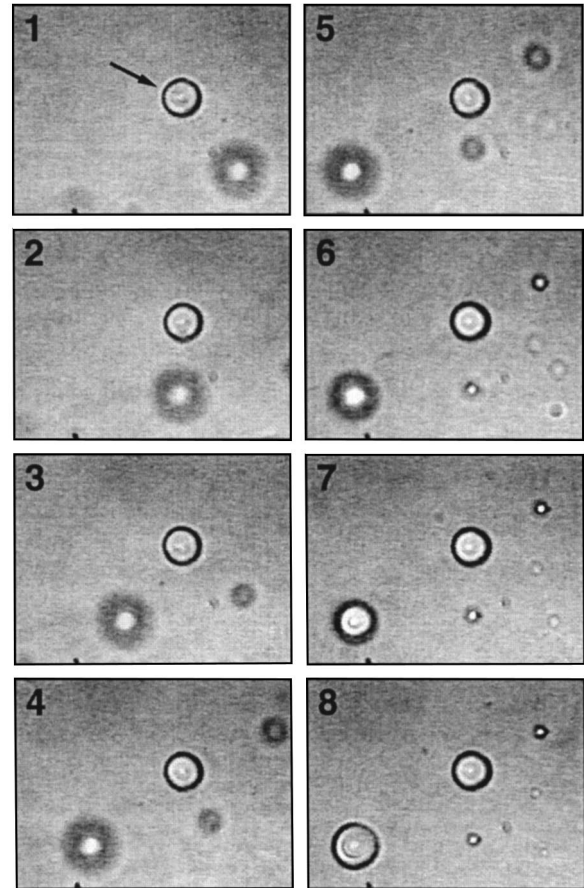


Fig. 11. Manipulation of a trapped water droplet in acetophenone (indicated by an arrow in the first frame). Transverse trapping is shown in the first four frames. Longitudinal trapping is shown in the remaining frames. Frame dimensions are 50 \times 30 μm . The time for each frame is sequential, but not linear. The total time is approximately 10 s.

same position in each frame while nearby untrapped particles, initially out of focus, are observed to move, first to the left (in frames 1–4) and then into the focal plane (in frames 5–8), demonstrating both transverse and longitudinal trapping.

An incident beam power of $P \approx 100\text{--}500$ mW was necessary to achieve robust trapping for the HGS system, while $P \approx 50\text{--}100$ mW was needed for a similar level of stability in the H_2O –acetophenone system. This difference may be attributed to the greater buoyancy of the HGS particles. Transverse velocities up to $50 \mu\text{m/s}$ and longitudinal velocities of $30 \mu\text{m/s}$ were estimated from videotaped sequences. Furthermore, at a given power level, higher longitudinal velocities were possible when translating droplets upward (in the $-z$ direction), rather than downward. While buoyancy may contribute to this bias, particularly in the HGS system, the fact that the effect was also observed in the nearly density-matched H_2O –acetophenone system suggests that a larger restoring force is exerted from below the droplet as predicted by the RO model [see Fig. 4(a)].

We observed with the H_2O –acetophenone system that both rapid movement of trapped water droplets and high incident-beam power caused the droplets to shrink while in the trap. The resulting decrease in droplet size was immediately evident as a noticeable defocusing of the droplet image. This behavior was observed for incident-beam powers of a few tens of milliwatts ($E_0 \approx 10^6$ V/m) and at translation speeds greater than $\sim 20 \mu\text{m/s}$. Although the mechanism is unclear, we suspect that shrinkage may result from the droplet's dissolving into the acetophenone or the formation of a microemulsion of water droplets. This feature may be exploited to accurately measure the stable trapping position over a range of droplet sizes without having to recalibrate the position of the beam focus each time a measurement is made.

Measurements of the stable trapping position z_{trap} as a function of particle radius R_p were performed for both low-index particle systems. Figures 12(a) and 12(b) plot the measured trapping position for the H_2O –acetophenone and HGS systems, respectively. Consistent with the RO model, a linear relationship between z_{trap} and R_p is evident for both systems. A linear fit to the data yields slopes of $z_{\text{trap}}/R_p = -2.67$ for the H_2O –acetophenone system and $z_{\text{trap}}/R_p = -2.22$ for the HGS system. In both cases, the linear fit intercepts the vertical axis within the $\pm 2 \mu\text{m}$ uncertainty of the z_{trap} measurement. From our discussion of the RO model in Subsection 2.C, we may expect the slope to be almost exclusively determined by the relative refractive index m of the particle. Comparing the measured slope with RO calculations presented in Fig. 8(a), an estimated relative refractive index of $m = 0.88$ is found for the H_2O –acetophenone system. Refractive-index measurements at a slightly shorter wavelength of 489 nm (the sodium D line) obtained from the Merck Index give $m = 1.33/1.53 = 1.33/1.53 = 0.87$ for this system, which is within 2% of our estimated value. In comparison, an estimate of $m = 0.84$, obtained from experimental data for the HGS system, agrees to within 10% of the limiting value of $m = 0.75$ for an air bubble in water [represented by the dashed line in Fig. 12(b)]. The calculation of an effective

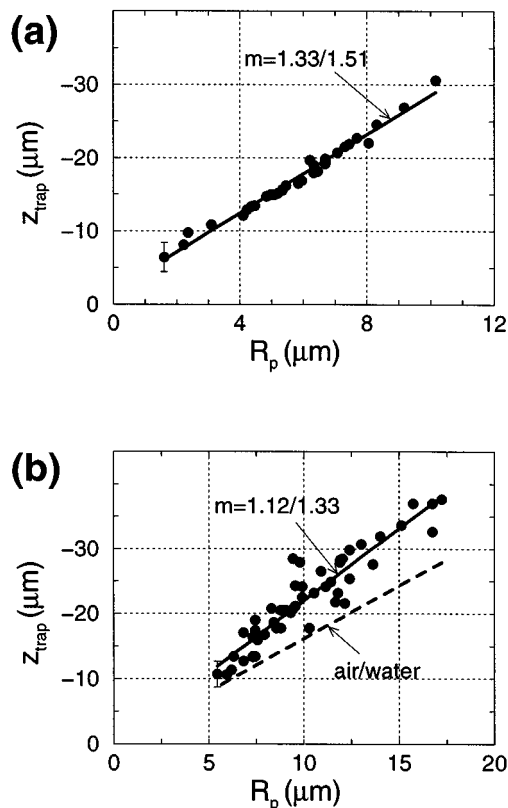


Fig. 12. Stable trapping position measured as a function of particle radius for (a) the HGS system and (b) the H_2O –acetophenone system. Solid lines indicate a linear least-squares fit to the measured data. Dashed line indicates RO calculation for the limiting case of an air bubble in water.

refractive index, which accounts for the nonzero thickness of the glass shell, is complicated by an angular dependence of the optical path length through the shell, particularly for rays incident at large α . Nevertheless, for the case of a thin shell, we may expect that the presence of the glass ($n = 1.52$) will tend to increase slightly the refractive index of the sphere. With particles much smaller than the wavelength, the calculation of an effective index of refraction for a shell particle is straightforward⁴⁰ and provides a rough estimate for large particles, as long as structural resonances are avoided. Assuming a wall thickness $t = 0.05R_p$, this method yields an effective relative refractive index of $m_{\text{eff}} = 0.80$, which differs approximately 5% from the value obtained from measured data.

We investigated qualitatively the effect of varying the relative vortex core size η and NA on the stability and stable trapping position. No shift in z_{trap} was evident within the resolution of our measurements over a range of $0.1 < \eta < 0.3$. Note: For a “donut” Laguerre–Gaussian laser mode, $\eta \approx 2.0$. This finding is in agreement with Fig. 6(a), in which it is shown that the RO model predicts little change in z_{trap} with η . However, the value of η does affect the stability of the trap. For the smallest particles studied ($2\text{--}5 \mu\text{m}$), a value of $\eta \approx 0.25$ was optimal, whereas for larger particles smaller values of η were sufficient. This trend is consistent with the RO model, as noted in Section 2. The effective NA of the objective was

varied by narrowing the Gaussian-beam waist at the input aperture. We observed that narrowing the beam waist by a small amount, approximately 10%–20%, increased the longitudinal stability of the trap for larger particles but destabilized the trap transversely for small particles. Further narrowing of the beam waist destabilized the trap in the transverse direction for both large and small particles.

4. DISCUSSION

We have experimentally demonstrated optical-vortex trapping of both buoyant and neutral-density particles whose refractive index is lower than that of the host fluid. Numerical solutions based on the RO model for large particles gave accurate predictions of the stable trapping position and produced qualitative agreement with efficiency trends observed for different beam profiles.

We found that by varying the vortex-core size or NA of the optical system, the maximum trapping efficiency in either the transverse or the longitudinal direction could be enhanced. The use of CGH methods in combination with beam expanders and condensers for preparing the input beam profile permits relatively easy adjustment of these parameters. The optimum trapping configuration will differ for different trapped species, owing to other factors affecting the trapping efficiency such as particle size, buoyancy, or absorption. For example, buoyant particles may require values of $Q_{z,\max}$ larger than $Q_{\rho,\min}$. Optimizing the efficiency may even be counterproductive in some cases. For instance, small particles are subject to greater relative displacements than are large particles because of Brownian motion, and thus an increased trap width may be preferred. Shifting z_{trap} away from the beam focus (for example, by decreasing the refractive index of the host liquid) will widen the trap, although the trapping efficiency may also decrease.

The OVT may provide a means of investigating the properties of a variety of low-index particle systems. Emulsion systems, in particular, are interesting candidates. For instance, when combined with coherent light-scattering particle-size measurements in a manner similar to that recently demonstrated by Lankers *et al.*,⁵ the vortex trap may be used to study evaporative and other interfacial processes of water-in-oil emulsions with great precision.

Finally, much interest has been devoted recently to the study of angular-momentum transfer to absorbing particles in optical levitation and trapping configurations.^{24,23} The transfer of angular momentum, whether from optical vortices (orbital angular momentum) or circularly polarized light (spin angular momentum) is proportional to the absorption coefficient of the particle. A large absorption coefficient increases the rate of angular momentum transfer but also increases linear momentum transferred to the particle along the propagation direction of the incident light, destabilizing optical traps for high-index particles for which the restoring force is weaker on the lower side of the trap. In contrast, the strong gradient force exerted on low-index particles below the stable position may accommodate larger absorption coefficients before trap destabilization results. We pro-

pose that increased angular momentum transfer may be achieved by use of low-index particles trapped within an optical vortex in the manner described in this paper.

5. CONCLUSIONS

We have investigated three-dimensional optical trapping of low-index microparticles with a focused optical-vortex beam, both theoretically and experimentally, for two particle systems: an emulsion of water droplets in acetophenone and HGS's in water. A simplified RO model of radiation pressure, valid for large particles, is shown to predict a stable trapping position for low-index particles at a point located on the optical axis at a distance of 2 to 3 times the particle radius before the beam focus. The influence of parameters, such as the width of the vortex core, the NA of the focusing objective, and the relative refractive index of the particle system, on the location of the stable point and the trapping efficiency have been examined. The distance of the stable point from the beam focus, z_{trap} , is expected to scale linearly with the particle radius R_p by a factor that depends primarily on the relative refractive index m of the particle. This dependence was verified experimentally for both low-index particle systems over a range of particle diameters of 5 to 40 μm . Scaling factors of $z_{\text{trap}}/R_p = -2.67$ and $z_{\text{trap}}/R_p = -2.22$, measured for the H_2O –acetophenone and HGS systems, respectively, are within a few percent of the RO calculations. A trend of increased longitudinal efficiency and decreased transverse efficiency with decreasing core size η and NA, predicted by the model, was verified qualitatively in the experiment. In addition, trapping of smaller particles was found to be more sensitive to decreases in η and NA. A more detailed model, which accounts for particle size, is needed to examine this dependence further.

In closing, our numerical calculations of the trapping efficiency show that an OVT differs from a conventional Gaussian trap in several ways. For instance, both low- and high-index particles are easily trapped with the same vortex configuration, whereas for a conventional trap only trapping of high-index particles has been demonstrated. In addition, trapping of low-index particles within the dark vortex core permits isolation of a single particle in the transverse direction. Finally, given the improved efficiency of OVT's for high-index particles and the reduced risk of optical damage, we believe this design is more versatile and easier to implement than other proposed methods for microparticle trapping.

ACKNOWLEDGMENTS

This research was supported by the National Science Foundation (Young Investigator Award), the Research Corporation (Cottrell Scholars Award), Spectra-Physics Lasers, Inc., and the Newport Corporation. We are grateful for material and equipment contributions from Mark O. Freeman (Industrial Technology Research Institute, Hsinchu, Taiwan) and Donald F. Nelson and Elizabeth Ryder (Worcester Polytechnic Institute).

REFERENCES

1. A. Ashkin, J. M. Dziedzic, J. E. Bjorkholm, and S. Chu, "Observation of a single-beam gradient force optical trap for dielectric particles," *Opt. Lett.* **11**, 288–290 (1986).
2. B. T. Unger and P. L. Marston, "Optical levitation of bubbles in water by the radiation pressure of a laser beam: an acoustically quiet levitator," *J. Acoust. Soc. Am.* **83**, 970–975 (1988).
3. J. C. Crocker and D. G. Grier, "Microscopic measurement of the pair interaction potential of charge-stabilized colloid," *Phys. Rev. Lett.* **73**, 352–355 (1994).
4. G. Roll, T. Kaiser, and G. Schweiger, "Optical trap sedimentation cell—a new technique for the sizing of microparticles," *J. Aerosol Sci.* **27**, 105–117 (1996).
5. M. Lankers, E. E. M. Khaled, J. Popp, G. Rössling, H. Stahl, and W. Kiefer, "Determination of size changes of optically trapped gas bubbles by elastic light backscattering," *Appl. Opt.* **36**, 1638–1643 (1997).
6. W. H. Wright, G. J. Sonek, Y. Tadir, and Michael W. Berns, "Laser trapping in cell biology," *IEEE J. Quantum Electron.* **26**, 2148–2157 (1990).
7. A. Ashkin, J. M. Dziedzic, and T. Yamane, "Optical trapping and manipulation of single cells using infrared laser beams," *Nature (London)* **330**, 769–771 (1987).
8. F. Hoffmann, "Laser microbeams for the manipulation of plant cells and subcellular structures," *Plant Sci.* **113**, 1–11 (1996).
9. C. S. Buer, K. T. Gahagan, G. A. Swartzlander, Jr., and P. J. Weathers, "Threshold of power for *Cucumis melo* using an Ar⁺ laser beam," *In Vitro Cellular and Developmental Biology—Animal* **32** (Part II), 82A (1996).
10. Y. Tadir, W. H. Wright, O. Vafa, R. Asch, and M. W. Berns, "Force generated by human sperm correlated to velocity and determined using a laser generated optical trap," *Fert. Ster.* **53**, 944–947 (1990).
11. K. Svoboda and S. M. Block, "Force and velocity measured for single kinesin molecules," *Cell* **77**, 773–784 (1994).
12. P. J. H. Bronkhorst, G. J. Streekstra, J. Grimbergen, J. Nijh, J. J. Sixma, and G. J. Brakenhoff, "A new method to study shape recovery of red blood cells using multiple optical trapping," *Biophys. J.* **69**, 1666–1673 (1995).
13. M. Schindler, "The cell optical displacement assay (coda): measurements of cytoskeletal tension in living plant cells with a laser optical trap," *Methods Cell Biol.* **49**, 71–84 (1995).
14. A. Ashkin and J. M. Dziedzic, "Optical trapping and manipulation of single living cells using infra-red laser beams," *Ber. Bunsenges. Phys. Chem.* **93**, 254–260 (1989).
15. I. A. Vorobjev, H. Liang, W. H. Wright, and M. W. Berns, "Optical trapping for chromosome manipulation: a wavelength dependence of induced chromosome bridges," *Biophys. J.* **64**, 533–538 (1993).
16. K. Konig, H. Liang, M. W. Berns, and B. J. Tromberg, "Cell damage in near infrared multimode optical traps as a result of multiphoton absorption," *Opt. Lett.* **21**, 1090–1092 (1996).
17. K. Svoboda and S. M. Block, "Optical trapping of metallic Rayleigh particles," *Opt. Lett.* **19**, 930–932 (1994).
18. J. F. Nye and M. V. Berry, "Dislocations in wave trains," *Proc. R. Soc. London, Ser. A* **336**, 165–190 (1974).
19. V. Y. Bazhenov, M. S. Soskin, and M. V. Vasnetsov, "Screw dislocations in light wavefronts," *J. Mod. Opt.* **39**, 985–990 (1992).
20. A. Ashkin, "Forces of a single-beam gradient trap on a dielectric sphere in the ray optics regime," *Biophys. J.* **61**, 569–582 (1992).
21. S. Sato, M. Ishigure, and H. Inaba, "Application of higher-order-mode Nd:YAG laser beam for manipulation and rotation of biological cells," in *Conference on Lasers and Electro-Optics*, Vol. 10 of OSA Technical Digest Series (Optical Society of America, Washington, D.C., 1991), pp. 280–281.
22. N. B. Simpson, K. Dholakia, L. Allen, and M. J. Padgett, "Mechanical equivalence of spin and orbital angular momentum of light: an optical spanner," *Opt. Lett.* **22**, 52–54 (1997).
23. H. He, N. R. Heckenberg, and H. Rubinsztein-Dunlop, "Optical particle trapping with higher-order doughnut beams produced using high efficiency computer generated holograms," *J. Mod. Opt.* **42**, 217–223 (1995).
24. H. He, M. E. J. Friese, N. R. Heckenberg, and H. Rubinsztein-Dunlop, "Direct observation of transfer of angular momentum to absorptive particles from a laser beam with a phase singularity," *Phys. Rev. Lett.* **75**, 826–828 (1995).
25. M. E. J. Friese, J. Enger, H. Rubinsztein-Dunlop, and N. R. Heckenberg, "Optical angular-momentum transfer to trapped absorbing particles," *Phys. Rev. A* **54**, 1593–1596 (1996).
26. N. B. Simpson, L. Allen, and M. J. Padgett, "Optical tweezers and optical spanners with Laguerre-Gaussian modes," *J. Mod. Opt.* **43**, 2485–2491 (1996).
27. D. Rozas, C. T. Law, and G. A. Swartzlander, Jr., "Propagation dynamics of optical vortices," *J. Opt. Soc. Am. B* **14**, 3054–3065 (1997).
28. D. Rozas, Z. S. Sacks, and G. A. Swartzlander, Jr., "Experimental observation of fluid-like motion of optical vortices," *Phys. Rev. Lett.* **79**, 3399–3402 (1997).
29. K. T. Gahagan and G. A. Swartzlander, Jr., "Optical vortex trapping of particles," *Opt. Lett.* **21**, 827–829 (1996).
30. K. Sasaki, M. Koshioka, H. Misawa, N. Kitamura, and H. Masuhara, "Optical trapping of a metal particle and a water droplet by a scanning laser beam," *Appl. Phys. Lett.* **60**, 807–809 (1992).
31. E. Higurashi, H. Ukita, H. Tanaka, and O. Ohguchi, "Optically induced rotation of anisotropic micro-objects fabricated by surface micromachining," *Appl. Phys. Lett.* **64**, 2209–2210 (1994).
32. E. Higurashi, O. Ohguchi, and H. Ukita, "Optical trapping of low-refractive-index microfabricated objects using radiation pressure exerted on their inner walls," *Opt. Lett.* **20**, 1931–1933 (1995).
33. J. P. Barton and D. R. Alexander, "Fifth-order corrected electromagnetic field components for a fundamental Gaussian beam," *J. Appl. Phys.* **66**, 2800–2802 (1989).
34. W. H. Wright, G. J. Sonek, and M. W. Berns, "Parametric study of the forces on microspheres held by optical tweezers," *Appl. Opt.* **33**, 1735–1748 (1994).
35. K. F. Ren, G. Gréhan, and G. Gouesbet, "Radiation pressure forces exerted on a particle arbitrarily located in a Gaussian beam by using the generalized Lorenz-Mie theory, and associated resonance effects," *Opt. Commun.* **108**, 343–354 (1994).
36. G. Roosen and C. Imbert, "Optical levitation by means of 2 horizontal laser beams: theoretical and experimental study," *Phys. Lett.* **59A**, 6–8 (1976).
37. R. Gussgard, T. Lindmo, and I. Brevik, "Calculation of the trapping force in a strongly focused laser beam," *J. Opt. Soc. Am. B* **9**, 1922–1930 (1992).
38. H. C. van de Hulst, *Light Scattering by Small Particles* (Wiley, New York, 1957), pp. 208–215.
39. A. Ashkin and J. M. Dziedzic, "Stability of optical levitation by radiation pressure," *Appl. Phys. Lett.* **24**, 586–588 (1974).
40. Ref. 38, pp. 73–74.